aerospace

MDPI

Article

Preliminary Design of a Tandem-Wing Unmanned Aerial System †

Alejandro Sanchez-Carmona, Daniel del Río Velilla, Antonio Fernández López and Cristina Cuerno-Rejado *

Escuela Técnica Superior de Ingeniería Aeronáutica y del Espacio, Universidad Politécnica de Madrid, 28040 Madrid, Spain; alejandro.sanchezc@upm.es (A.S.-C.); daniel.delrio.velilla@upm.es (D.d.R.V.); antonio.fernandez.lopez@upm.es (A.F.L.)

* Correspondence: cristina.cuerno@upm.es

† This paper is an extended version of our paper published in Cuerno-Rejado, C.; García-Hernández, L.; Sanchez-Carmona, A.; Fernández-López, A.; Pintado-Sanjuanbenito, J.M. Diseño Modular de un RPAS de ala Tándem de Despegue Vertical. In Proceedings of the CivilDRON'17, Fundación de la Energía de la Comunidad de Madrid, Madrid, Spain, 25–26 January 2017.

Abstract: The drone industry is continuously growing. The regulatory framework that allows these aircraft to operate safely is gradually evolving, enabling missions with growing associated risks, although it is not progressing at the same speed as the industry itself. To provide certainty to regulators, it is necessary to employ design methodologies that are recognized in the aerospace industry. Therefore, in this work, we addressed the design and manufacturing of a lightweight unconventional-configuration unmanned aircraft by adapting widely known conceptual design methodologies from manned aviation from authors such as Torenbeek and Roskam. Manufacturing was carried out by combining new techniques for the use of composite materials with additive manufacturing. A wide variability in the results was identified across the different models used. However, taking the most restrictive estimates into account, the results show that the structural weight estimates of the wing, made using classical manned aviation methods, align with the final weight obtained, assuming the wing can withstand the aerodynamic and inertial loads applied within a certain safety margin.

Keywords: UAS; conceptual design; tandem wing; additive manufacturing; structuralizing

Academic Editor: Dimitri Mavris

Received: 12 March 2025
Revised: 14 April 2025
Accepted: 18 April 2025
Published: 22 April 2025

Citation: Sanchez-Carmona, A.; del Río Velilla, D.; Fernández López, A.; Cuerno-Rejado, C. Preliminary Design of a Tandem-Wing Unmanned Aerial System. *Aerospace* **2025**, *12*, 363. https://doi.org/10.3390/aerospace12050363

1. Introduction

Unmanned aircraft currently constitute an emerging market within the aerospace industry. Although this type of aircraft is nearly as old as conventional aviation, which requires onboard pilots, throughout most of the 20th century, its design and use remained largely in the hands of military forces. These forces recognized early on the advantages that this type of aviation could offer for numerous military applications. However, at the end of the 20th century and into the 21st century, the civilian and commercial sectors became and remain, respectively, the primary drivers of expansion for unmanned aircraft.

Today, the number of possible missions, aircraft configurations, weight categories, and performance capabilities appears to have no limits. Extensive bibliographic references are available, providing comprehensive descriptions of the various types of unmanned aircraft, their key characteristics, and numerous examples of potential missions they can undertake [1–7].

We are currently witnessing the unstoppable evolution of this sector, driven by continuous technological advancements that enable missions to be carried out with increasing

efficiency and reliability. Meanwhile, the regulatory framework necessary to conduct unmanned aircraft operations under safety conditions equivalent to those of manned aviation is advancing gradually. However, regulatory progress remains slower compared to the rapid pace of advancement in technological capabilities [8,9].

In recent years, various studies on unmanned aerial system (UAS) design have been published in the open literature. The following text includes a collection of bibliographic references showcasing different design examples. These works, along with others not cited here but available in the open literature, demonstrate the feasibility of developing innovative unmanned aircraft concepts suitable for a wide range of missions. However, despite these examples, there is a notable lack of well-established design methodologies that comprehensively address the various phases of aircraft design, particularly the conceptual and preliminary design stages, in which the main parameters regarding the initial sizing and main performance are established.

In recent years, several studies related to UAS design have been published, highlighting an appropriate combination of an initial design methodology with a specific application in an "ad hoc" design. For example, the work by Panagiotou et al. [10] focuses on the aerodynamic design of a MALE UAS. The study by Kontogiannis and Ekaterinaris [11] addresses the development of a small-category UAS, carrying the design process through to prototype manufacturing and flight testing.

Additionally, some studies explored highly specific designs tailored for particular missions. For instance, the research by Bravo-Mosquera et al. [12] involved the design of a UAS optimized for volcanic environments, while Goetzendorf-Grabowski and Rodzewicz [13] developed a UAS for operations in the Antarctic region. Other authors designed and subsequently redesigned fixed-wing convertible UASs, whereas Panagiotou, Fortiadis-Karras, and Yakintos [14] focused on the conceptual design of a UAS with an unconventional "Blended Wing Body" configuration.

Following this trend of unconventional configurations, the work by Vittorio Cipolla et al. [15] stands out. They applied box-wing and tandem-wing concepts to the design of a small, solar-powered UAS. Furthermore, there are highly innovative studies, such as those by Xin Zhao, Zhou Zhou, Xiaoping Zhu, and A. Guo [16], which present the design of a hand-launched solar-powered UAS. Similarly, Jae-Hyun An, Do-Youn Kwon, Kwon-Su Jeon, Maxim Tyan, and Jae-Woo Lee [17], as well as Siwat Suewatanakul et al. [18], proposed the design of electric UASs powered by hydrogen fuel cells and batteries. Lastly, Peter L. Bishay et al. [19] applied "morphing" techniques to UAS design, demonstrating further advancements in this field.

The work presented in this document involves the configuration and complete design—culminating in the fabrication of an initial prototype—of an unconventional unmanned aircraft. The origins of this design trace back to a challenge made in collaboration with aerospace manufacturers Airbus and Local Motors in 2016. This challenge, called the Cargo Drone Challenge [20], was an international design competition that required participants to propose solutions meeting a set of predefined requirements. One of the key constraints was that the aircraft had to be capable of transporting a specific payload within a container of a prefixed size. To address this challenge, we carried out the aircraft design process presented in this paper.

To successfully develop the design of the aircraft, it was necessary to establish a structured design methodology. This methodology was based on existing conceptual and preliminary design methods for manned transport aircraft, which were then adapted to meet the specific requirements of this project [21–30].

In addition to the methodology outlined in this document, an innovative approach was employed to adapt traditional carbon-fiber aircraft structure manufacturing techniques.

This was achieved by developing a novel process for creating master molds using additive manufacturing (3D printing). To determine the final dimensions and create production drawings for the master molds, we incorporated innovative approaches into the conceptual design process to establish the primary design loads. These calculations considered key aircraft performance parameters and existing certification standards for unmanned aircraft based on NATO regulations [31].

The conclusions of this work are highly positive. The research team successfully conceived a complete aircraft design and fabricated a prototype with a high level of quality, comparable to other aircraft in this category. The team is now taking the steps necessary to conduct flight testing, which will provide more precise performance data and validate the aircraft's compliance with the initial design specifications.

2. Materials and Methods

The aircraft design methodology followed in this paper is based on a set of initial specifications or design requirements. These requirements define, in various ways, the equipment needed to carry out UAS missions. First, the fuselage is sized to accommodate the equipment to be carried. Next, an estimate of the aircraft's weight is made based on the payload and the onboard equipment. This estimation is based on statistical correlations developed from similar aircraft for which sufficient information is available. The estimated weights include the maximum takeoff weight and the operational empty weight. With this information, the design point of the aircraft can be determined, which essentially involves selecting the power-to-weight ratio and the wing loading based on various design criteria. Once the design point is known, the complete geometry of the aircraft can be obtained, meaning the wings, vertical tail surfaces, and landing gear can be sized. At this stage, the aircraft weights are estimated in more detail, as the weight of each structural component can be determined according to class 2 methods [30,32]. In turn, the aircraft's center of gravity is calculated, as it will be necessary for the subsequent aerodynamic calculations. These calculations help determine the lift curve, the moment curve, and the drag polar of the UAS. Additionally, stability derivatives are estimated, as some of them will be necessary to ensure the requirements related to headwinds and crosswinds are met. The final step in the design process is to select the propulsion system. This step is particularly important because the propulsion system consists of batteries, speed controllers, electric motors, and fixed-pitch propellers. The goal is to find a combination of these elements that optimally fulfills the requirements of the design mission. Therefore, it is essential to recalculate the aircraft's performance once the final propulsion system is selected.

The design process is iterative, with several feedback loops. The first of these is the weight loop. Here, the aim is to make the initial weight estimate required for the design-point phase converge with the more detailed estimate made once the aircraft geometry is known. Once this loop has converged, a new iteration is carried out between the design point and the aerodynamics, as determining the design point requires an estimate of the aircraft's drag polar, which must closely match the drag polar obtained at the end of the aerodynamic phase. This loop is unique in that it contains the weight loop within it, meaning that in each iteration step, the weight loop must also converge. Thus, the process of convergence between the weight and aerodynamic loops is simultaneous. Converging the aerodynamics and weights involves establishing the mass distribution along the fuselage to keep the center of gravity in a position that provides an acceptable static margin with fixed controls. Therefore, the iterations are fed back with C_L (lift coefficient) and C_M (pitching moment coefficient) curves as a function of the angle of attack. The other stability derivatives are checked afterward, once the entire design process has converged.

Finally, once both loops have converged, it will be necessary to select the propulsion system, i.e., the battery, speed controller, motor, and propeller combination that allows the design mission to be carried out. Again, this process is iterative or trial and error until the combination that best meets the performance requirements is found. Figure 1 shows this process described previously.

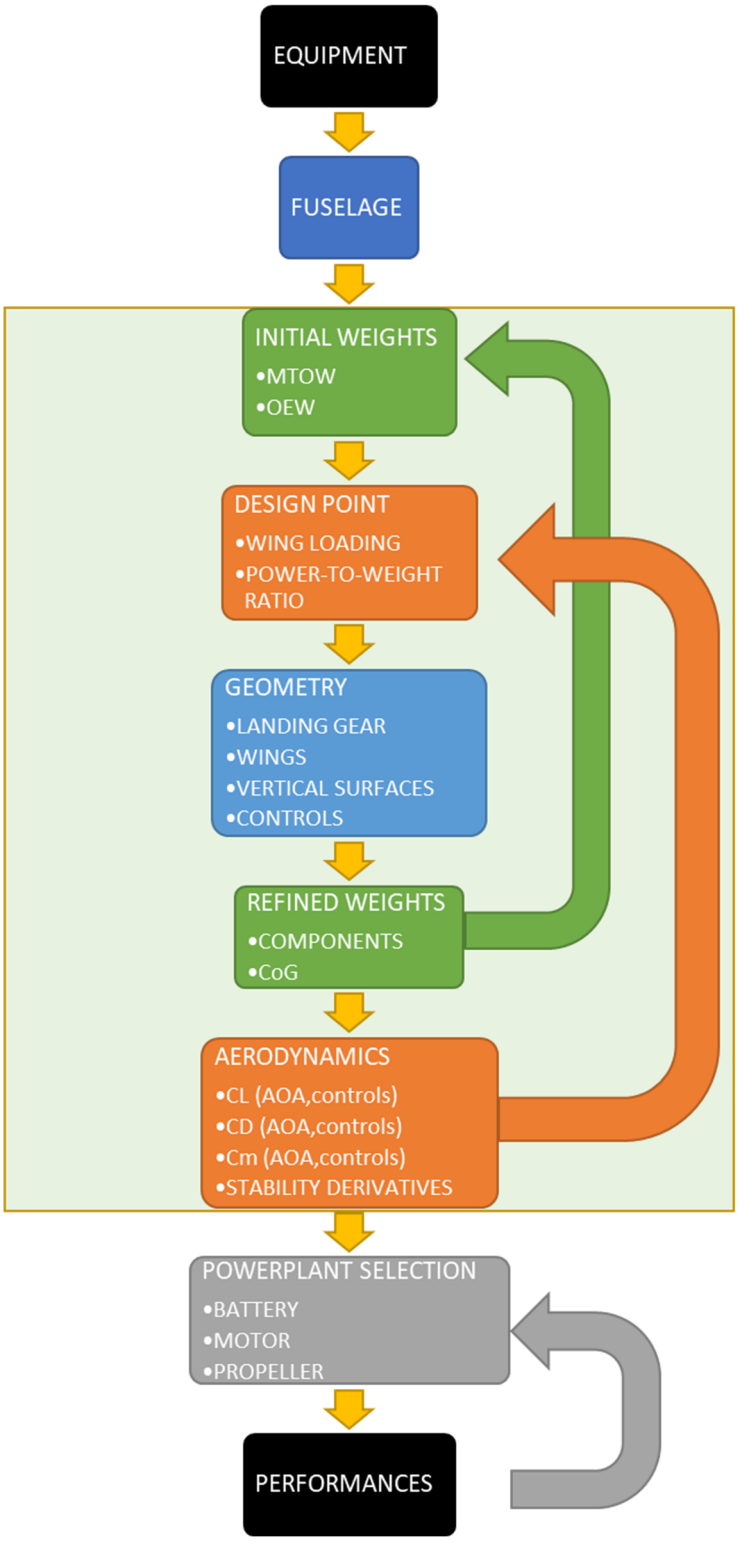

Figure 1. The design process followed in this work.

3. Case Study: Tandem-Wing UAS

In this section, we present a case study developed to show how the design methodology described previously can be applied. The preliminary results of this research were presented at the CivilDRON'17 conference [33], but in this study, a deeper analysis was conducted in terms of flight envelope, loads, structural design, and manufacturing.

The results presented here were obtained after applying the design process described previously. Since the process was iterative, only the final results are shown. To determine the necessary statistical correlations (primarily useful in the first iteration of weight and aerodynamic analysis), data for UASs with less than 12 h of endurance and for single-engine, propeller-driven aircraft with fixed landing gear were used [34]. From there, the parameters, weights, and polar drag values were fed back into the results obtained after each step of the iteration process within the design loop presented in the previous section.

The results, after the design loops converged, are presented, starting with the design requirements used, followed by the final fuselage geometry, the design point, and the rest of the geometry, aerodynamics, weights, and performance. It is important to emphasize that despite this order of presenting the results, the design process follows the explanation given in the previous section. Finally, a structural analysis was conducted to refine and, if necessary, confirm the weight estimates obtained, enabling the progression to the manufacturing phase.

3.1. Design Requirements

The design requirements for the case study are a combination of the "Cargo Drone Challenge" competition guidelines [20] and several others. The main objective was to design a UAS with vertical takeoff and landing (VTOL) capability, while including at least one fixed wing for cruise flight. Due to the European regulations currently under development, the maximum takeoff weight must remain below 25 kg. Additionally, modularity conditions are imposed to facilitate an aircraft's transport. The maximum length of any individual part must not exceed 2 m.

The design mission consisted of transporting a container with the payload inside (initially of a medical nature), with specific dimensions (450 $\times$ 350 $\times$ 200 mm), over a certain distance. If the weight of the payload is 5 kg, the minimum distance the aircraft must be able to transport it is 60 km. However, if the weight of the payload is 3 kg, this distance increases to 100 km. Furthermore, the design mission must be carried out in such a way that there is enough energy to execute a 5 min hold before landing, if necessary, providing reserve energy for contingencies. Finally, a minimum transition time from takeoff to cruise flight conditions and from cruise flight to landing equal to 1 min each is required.

In addition to range, performance requirements also affect the cruise speed, which must be above 80 km/h, and the maximum aircraft speed, which must be below 194 km/h. Lastly, the design must be able to withstand headwinds and/or crosswinds of 10 m/s.

Regarding onboard equipment, the fuselage must house a flight control computer, an inertial measurement unit, a transponder, antennas for communication, a pitot tube for speed measurement, an emergency parachute system, a camera system, and a communications system. The weights and dimensions of each of these components were taken into account to restrict the aircraft's design. Additionally, we equipped the aircraft with an inductive battery charging system, aiming to extend its range simply by placing charging bases at strategic points.

Considering all these constraints, a tandem-wing configuration with four rotors for vertical takeoff and landing and a pusher propeller for cruise flight as the fixed wing were chosen. We selected this configuration because of the favorable stall behavior it facilitates, as the aircraft is designed such that the front wing stalls before the rear one. Thus, when

the front wing stalls and loses lift, the rear wing does not, creating a moment imbalance that tends to pitch the aircraft down, reducing the front wing's angle of attack and allowing it to regain normal lift. Taking advantage of this tandem configuration, we installed the motors for hover flight at the tips of the wings, which is why there are four motors for vertical takeoff and landing.

3.2. Fuselage

The fuselage is divided into three parts: front, central, and rear. The front part is a semi-ellipsoid, where the avionics systems and camera are located. The central part is a rectangular prism with a rounded corners section. This part houses the payload, the batteries, the IMU, and the parachute system. The rear part has a rectangular–pyramidal form with a rounded corners section. This part houses the rear powerplant and the attachments for the rear wing and vertical stabilizers. The dimensions of the fuselage were obtained by imposing some constraints. The first one pertains to transportability. The total length of the fuselage cannot exceed 2 m. Then, the relation between the three parts of the fuselage was determined to be 25%, 50%, and 25% of the total length. By analyzing Table 1, where all the equipment dimensions are included, it becomes clear that the width and height of the prismatic part can be determined by increasing by a certain factor the volume occupied by that equipment. The final dimensions of the fuselage are included in Table 2. From the standpoint of the structural concept, the fuselage consists of a beam that bears the loads transmitted by the wings and is also responsible for supporting the equipment. In addition, this equipment is supported by frames, which bear no structural loads. The external geometry is defined by light skin.

Table 1. Equipment list dimensions.

	Length [mm]	Width [mm]	Height [mm]
Flight control computer	170	180	80
Internal measurement unit	100	30	40
ADS-B transponder	89	46	18
Antennas and externally mounted systems	-	-	-
Flight termination parachute	280	120	50
Flight termination system	200	55	55
Camera	97	95	97
Communication system	57	98	86
Payload	473	368	210
Induction system charger	174	94	43
Induction system coil	300	300	10

Table 2. Fuselage geometry.

	Length
Length	2.00 m
"Cylindrical zone" length	1.00 m
Nose length	0.50 m
Rear end length	0.50 m
Maximum width	0.42 m
Maximum height	0.33 m

3.3. Design Point and Geometry

The power-to-weight ratio and wing loading were selected by analyzing the various constraints imposed on the design, such as cruise flight or behavior in gusts. In this

case, four conditions were imposed: the power required for a cruise flight at a constant speed above 80 km/h, the power required for a climb at a constant speed and a given climb angle, and performance in gusts at both cruise speed and maximum speed in level, unaccelerated flight.

The limitations to cruise flight and climb were imposed such that they established a minimum value for the power-to-weight ratio for each wing loading value. As mentioned previously, the design process is iterative; therefore, the results from the final iteration are shown here. In this iterative process, the drag polar and design point were adjusted such that the results shown in Figure 2 were obtained. In this case, because of the shape of the drag polar, the flight conditions that maximize both range and endurance are close to each other, meaning the design, which is a transport mission, is also optimized for surveillance missions, where maximum endurance is prioritized.

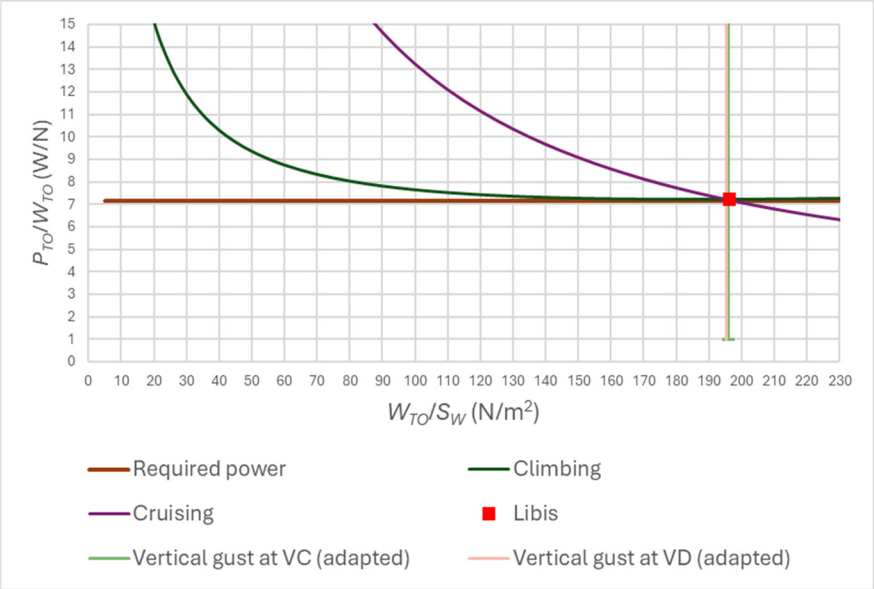

Figure 2. Design requirements introduced in the relationship between the power-to-weight ratio and wing loading.

Another limiting factor we considered is behavior in gusts. This limitation provides a minimum wing loading to ensure that the aircraft experiences a certain load factor at a given flight speed and gust intensity. The load factor imposed is the one typically used in regulations for military UASs [31] by means of the Pratt model [35]. The flight speeds considered are the design cruise speed and the maximum speed achievable in level flight. The drawback is that the airworthiness requirements code includes a gust intensity that, combined with the cruise speed, causes the aircraft to stall. Thus, it would not be reasonable to impose this load factor in the design to fulfill this requirement as it is set in the code. However, it is possible to adapt this requirement. First of all, the maximum gust intensity admissible for an aircraft is the minimum amount that leads to stalling conditions. Once this gust intensity is determined, the mathematical model can establish a relation between the wing loading and load factor. So, we decided to choose a wing loading that introduces a load factor that is lower or equal to 3.8, leading to wing loading limitations due to gusts.

Finally, a horizontal line representing the electric motor used to allow the UAS to fly as a fixed-wing aircraft is marked on the graph, with the selected point for the designed aircraft placed on this line. The point should be above the cruise and climb curves and to the right of the gust curves. This point was selected to allow a trade-off between satisfying all the constraints and obtaining a wing area (S_w) in order to make the manufacturing processes easier.

The procedure for obtaining the wing geometry is based on the results from the design point analysis, as the initial weight estimate allows the wing surface area to be determined. Once the wing surface area is known, the wing geometry can be set by imposing certain values on dimensionless quantities, such as the aspect ratio or taper ratio. Finally, the wing angles were set such that for the design cruise flight, the fuselage's angle of attack is zero and the aircraft's pitching moment is also zero without needing to deflect the rear-wing controls. The sizes of the vertical stabilizing surfaces were also set by imposing dimensionless values a priori, such as the vertical tail volume coefficient.

The size of the landing gear was set such that a series of basic requirements would be met, as information from similar aircraft could not be used. Some of these requirements include allowing the aircraft to land with a roll angle of 8° without the wing tips touching the ground or limiting the position of the nose gear for fuselage integration. The final layout of the whole geometry is shown in Figure 3.

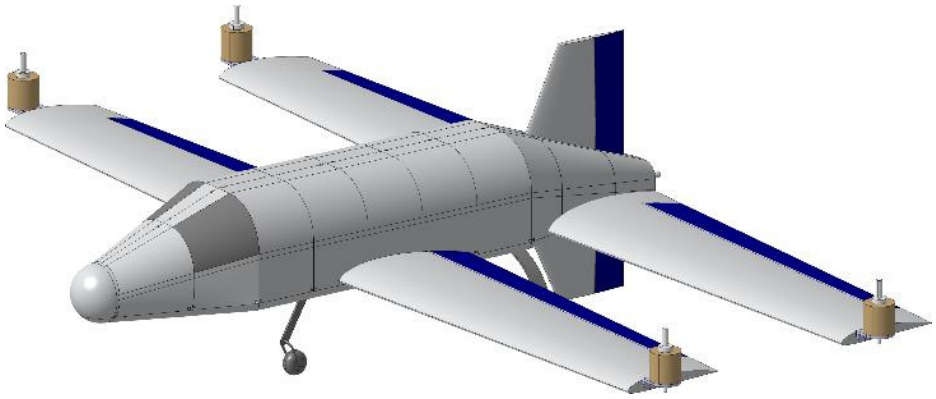

Figure 3. Final layout of the designed UAS.

3.4. Aerodynamics

The aerodynamics of the UAS were determined using several different methods: Torenbeek's method [21], Roskam's method [22,23,25–28,36], Raymer's method [30], and DATCOM [37]. All of these methods are classical procedures for estimating the aerodynamics of a commercial transport aircraft. The first three methods were appropriately modified to adapt them to small unmanned aerial vehicles, eliminating terms such as wave drag and adjusting the friction coefficients to the Reynolds number of the aircraft. The DATCOM method is a software product developed by McDonnell Douglas for the USAF; as such, it was not possible to adapt it to small UASs. Nevertheless, it was used for validation and comparison with the methods previously implemented. As shown in Figure 4, the DATCOM method is the most optimistic of all, as it predicts the best drag polar curve and the highest maximum aerodynamic efficiency. Torenbeek's method is reasonably similar to DATCOM with respect to lift coefficients below 0.5. In contrast, Roskam's and Raymer's methods are very similar to each other and predict the poorest drag polar curve and aerodynamic efficiency. Therefore, the results from Roskam's method were used for the subsequent iterations in order to be conservative in the estimation of the drag polar curve and aerodynamic efficiency (Figure 4). Furthermore, Roskam's method for determining drag polar was validated under several flight conditions for regional jets, even takeoff conditions with the landing gear extended, which could be the configuration and flight speed most similar to those for this UAS [38]. Under this condition, the differences in terms of aerodynamic coefficients, particularly the polar drag, between Roskam's method and flight tests are around 7%.

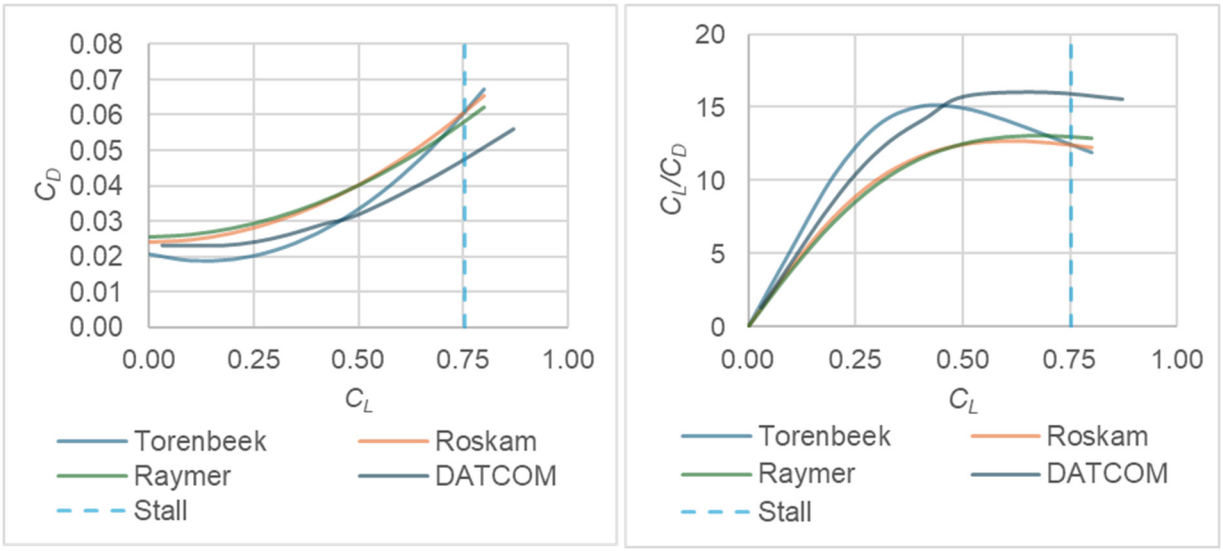

(**a**) (**b**)

Figure 4. (**a**) Drag polar curve (C_D vs. C_L) and (**b**) aerodynamic efficiency (C_L/C_D vs. C_L) for four different methods.

The stability derivatives presented in Figure 5 were calculated using different methods. Roskam's procedure is very similar to DATCOM; however, there are differences in the coefficients related to the rolling and yawing rates. In addition, DATCOM only admits NACA aerodynamic profiles, and Libis has a Clark-Y B profile. Due to this, the relative error between Roskam and DATCOM in certain longitudinal moments and rolling and yawing derivatives is higher [21,28,39]. As an additional evaluation, we estimated all these stability derivatives by means of AVL (Athena Vortex Lattice) software, version 3.35 for Windows. Developed at the Massachusetts Institute of Technology by Mark Drela, AVL is a program that allows one to perform aerodynamic and flight dynamic analyses of rigid aircraft with arbitrary configurations [40].

3.5. Weights

The final results regarding the aircraft's overall weights, including *MTOW* (maximum takeoff weight), *OEW* (Operative Empty Weight), and *BW* (Battery Weight), are presented for each *PL* (payload) in Figure 6. After completing the iterations, a difference of only 0.054% was found between the *OEWs* estimated in the general and detailed weight blocks, respectively, while the *MTOW* difference was 0.035%. Therefore, it can be concluded that the design process converged in terms of weight. The *MTOW* is 25 kg, and the *OEW* is 16.2 kg. In both payload cases, the takeoff weight reached the maximum value. The *OEW* is broken down into contributions from the fuselage, wings, vertical stabilizers, engines, landing gear, and avionics. It is important to note that the motors for vertical landing were selected based on the performance analysis presented in the next section. Furthermore, the estimates made for wing weight include control surfaces, servos, hinge shafts, the wing–fuselage joint, etc. However, the estimated structural weight of the wing is 907 g.

			ROSKAM & TORENBEEK	AVL	DATCOM	AVL RELATIVE ERROR	DATCOM RELATIVE ERROR
LONGITUDINAL STABILITY	0	C_{D0}	0.024	-	0.023	-	-4.79%
		C_{L0}	0.181	0.155	0.177	16.83%	-2.31%
		C_{m0}	-0.003	0.0114	-0.052	-76.30%	94.80%
	α	$C_{D\alpha}$	0.239	-		-	-
		$C_{L\alpha}$	4.138	4.038	4.245	2.48%	2.52%
		$C_{m\alpha}$	-0.707	-0.593	-0.944	19.21%	25.13%
	$\dot{\alpha}$	$C_{D\dot{\alpha}}$	0.000	-	-	-	-
		$C_{L\dot{\alpha}}$	7.411	-	-	-	-
		$C_{m\dot{\alpha}}$	-4.063	-	-	-	-
	q	C_{Dq}	0.000	-	-	-	-
		C_{Lq}	6.248	12.92	6.35	-51.64%	1.61%
		C_{mq}	-18.410	-27.78	-19.24	-33.73%	4.32%
	δ_e	$C_{D\delta e}$	0.005	-	-	-	-
		$C_{L\delta e}$	1.391	-	-	-	-
		$C_{m\delta e}$	-2.930	-	-	-	-
LATERAL-DIRECTIONAL STABILITY	β	$C_{Y\beta}$	-0.425	-0.395	-0.392	7.60%	-8.48%
		$C_{l\beta}$	-0.0286	-0.009	-0.0303	204.61%	5.53%
		$C_{n\beta}$	0.0170	0.025	0.0176	-31.91%	3.28%
	p	C_{Yp}	-0.004	0.0003	-0.00057	1208.69%	-586.38%
		C_{lp}	-0.472	-0.39	-0.493	21.14%	4.07%
		C_{np}	-0.019	-0.005	-0.006	271.75%	-199.80%
	r	C_{Yr}	0.120	0.28	-	-57.15%	-
		C_{lr}	0.049	0.027	0.032	82.22%	-52.04%
		C_{nr}	-0.040	-0.093	-0.052	-57.12%	23.32%
	δ_A	$C_{Y\delta A}$	0.000	-		-	-
		$C_{l\delta A}$	0.250	-		-	-
		$C_{n\delta A}$	-0.002	-		-	-
	δ_r	$C_{Y\delta r}$	-0.212	-		-	-
		$C_{l\delta r}$	-0.002	-		-	-
		$C_{n\delta r}$	0.051	-		-	-

Figure 5. Stability derivatives obtained by means of several methodologies, and a comparison of the results.

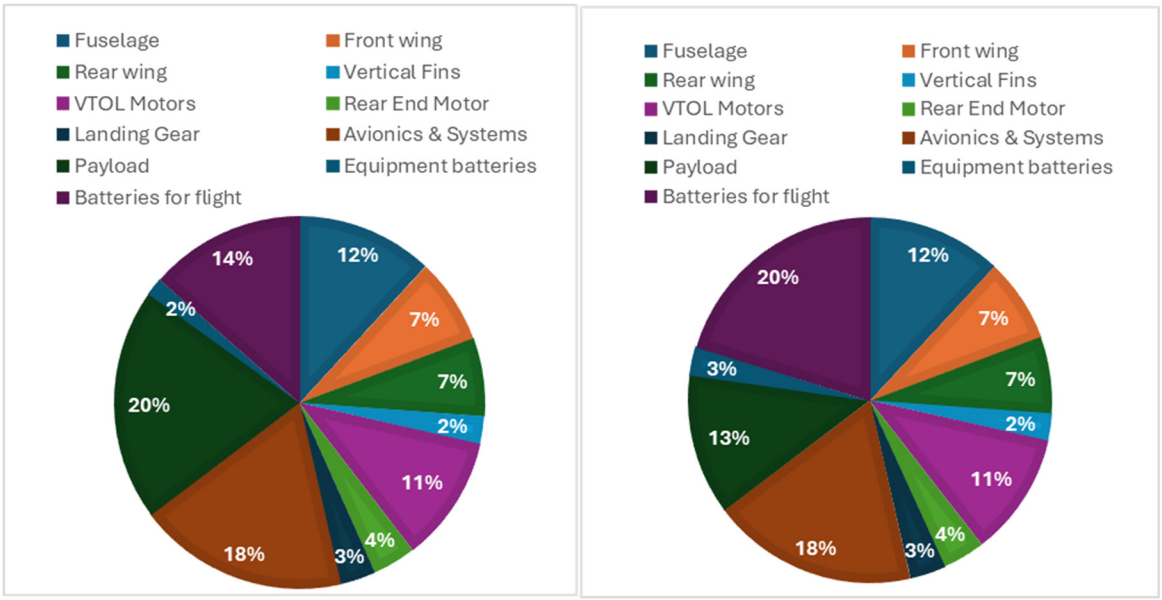

(**a**) (**b**)

Figure 6. Weight distributions for both missions: (**a**) PL = 5 kg and R = 60 km, and (**b**) PL = 3 kg and R = 100 km.

3.6. Performance

3.6.1. Design Mission

The design missions proposed in the challenge were carried out as follows:

1. Takeoff. As a rotary-wing aircraft, takeoff was executed from the ground to 300 feet with full throttle on VTOL motors.
2. Acceleration stage. This stage was divided into two sub-stages. First, the weight of the aircraft was lifted by the rotary wing, while the rear motor generated the aircraft's horizontal speed. During this stage, the angle of attack was kept in the minimum-drag position. This stage ended when the horizontal speed reached the stall speed. From this point, the power transmitted to the VTOL motors was reduced linearly until cruise speed was reached, at which point the VTOL motors were fully turned off. In this second stage, the angle of attack was changed to ensure that enough lift force was provided. At the end of this stage, lift was generated only by the fixed wings. The duration and energy consumption of this phase were carried out using a Runge–Kutta integration method. The horizontal distance traveled at this stage was considered.
3. Cruise flight. This was developed at maximum range speed.
4. Loiter. The aircraft loitered for 5 min at maximum endurance speed. Because maximum endurance speed and maximum range speed are very close to each other, we decided to fly the UAS at the same speed in both stages.
5. Descent stage. Descent was performed at a descent angle of 5º. The constant speed reached at this stage was 32.1 m/s. The descent ended when a height of 33 feet was reached.
6. Deceleration stage. The UAS decelerated from 32.1 m/s to 0 m/s. The hypotheses for this stage are like those for the acceleration stage.
7. Landing. As a rotary-wing aircraft, the UAS was landed by lowering it from 33 feet to the ground.

Schemas of the mission and the time and consumption analysis are included in Figure 7 and Table 3, respectively.

In order to choose the powerplants for VTOL, based on the required power for performing takeoff and landing maneuvers, the motor, battery, and propeller combination capable of executing these maneuvers with a certain safety margin was determined.

Table 3. Time analysis of the mission. When a slash appears in a cell, the left value applies for a 5 kg payload, and the right applies for a 3 kg payload. A hyphen in a cell indicates the variation interval of the magnitude.

	Phase	Duration [min]	Energy Consumption [Wh]	Horizontal Speed [m/s]	Vertical Speed [m/s]
1	Takeoff	0.76	54.32	0	2.5
2	Acceleration	0.13	9.86	0–23.11	0
3	Cruise	45.6/73.2	489/798	23.11	0
4	Loiter	5	37.25	23.11	0
5	Decent	0.48	1.76	31.98	−2.8
6	Deceleration	0.19	7.12	32.1–0	0
7	Landing	0.08	5.89	0	−2

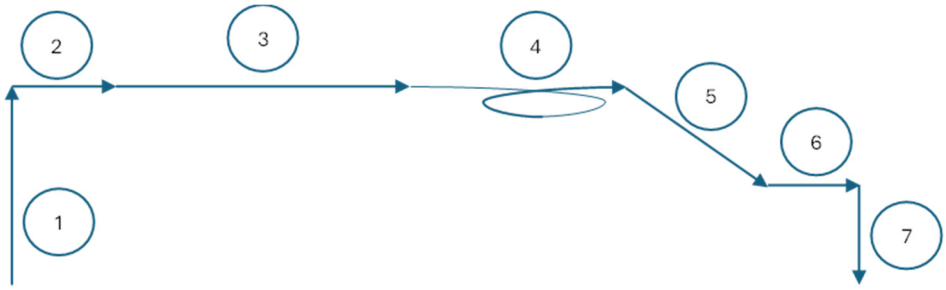

Figure 7. Mission flight profile.

3.6.2. Out–Off Design Mission

The modularity of this design allows the propulsion system to be changed depending on the required mission. Changes in the propulsion system imply changes in cruise speed, climb rate, and, consequently, aerodynamic efficiency. In addition, for each propulsion system configuration, it is possible to interchange the weight between the payload and batteries until the *MTOW* is reached. Since there are plenty of possibilities, shown here are only variations of the selected configuration for the design mission. Figure 8 provides payload–range and payload–endurance diagrams. These curves are theoretical since the equipment's battery does not change while endurance increases. In practice, the greater the endurance, the larger the equipment's battery must be.

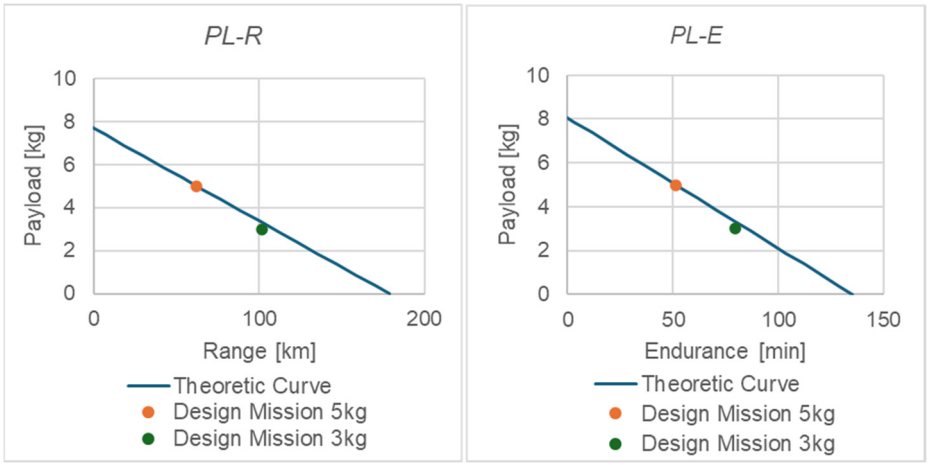

(**a**) (**b**)

Figure 8. (**a**) Payload vs. range diagram; (**b**) payload vs. endurance diagram.

Importantly, all the results related to the performance of the aircraft were calculated by making use of the tables of performance data from APC propellers [41] and AXI motors [42] via the program e-calc [43]. The curves provided by this program were evaluated against the available data provided by the manufacturer to ensure the results were accurate. Afterwards, the process carried out to obtain every cruising operating point consisted of balancing the required power for flying under cruising conditions and the power provided by the full powerplant, considering the performance of the battery, the motor, and the propeller. Battery efficiency was considered constant, although it depends on the temperature. The motor's efficiency and its angular rate depend on the feed current. Finally, propeller efficiency depends on the flying speed and the angular rate, as per the APC.

3.6.3. Wind Conditions and Flight Envelope

The ability of the UAS to achieve sustained flight while experiencing 10 m/s head and crosswinds was a requisite of the design mission. A study was conducted in order to

find a rudder deflection that satisfies this requirement. The result of this study showed that a deflection of the rudder (δ_r) of 7.8 degrees is sufficient to keep the yawing moment due to these crosswinds under the design mission conditions null. The ratio of horizontal speed to crosswinds for the design mission resulted in an angle of sideslip (β) of 23.4º. A headwind only affects aerodynamic velocity, so this affects the range that an aircraft can achieve. In the case of wind blowing from the rear, the range increases to 69.8 km for a 5 kg *PL* or 113.9 km for a 3 kg *PL*. On the other hand, if the wind blows from the front, the range decreases to 54.8 km for a 5 kg *PL* or 89.4 km for a 3 kg *PL*.

In Figure 9, the maximum supported gust intensity is shown on the left-hand side. This vertical speed induces an angle of attack and an increase in the load on the wings. The blue line is the maximum gust intensity that satisfies the load factor of 3.8 established by regulations for symmetric maneuvering conditions. The horizontal green line is the gust intensity that induces a stall angle of attack in the front wing at the chosen cruise speed. For this last calculation, a simple model considering that all wings experience the same vertical gust speed was used. On the right-hand side of the same figure, the rudder deflection required to negate the yawing moment in the presence of a crosswind is illustrated.

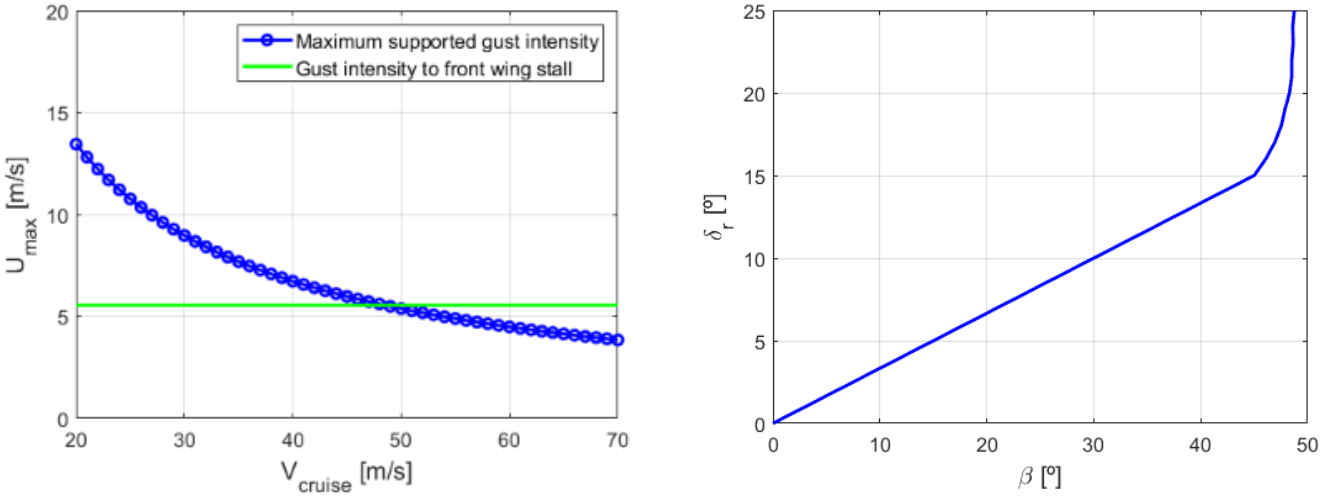

Figure 9. The maximum borne gust intensity with cruise speed (**left**) and rudder deflection with sideslip angle required to negate the yawing moment (**right**).

The flight envelope obtained is based on military regulations [31] because there are no civil requirements applicable to this aircraft that specify the constraints for the flight envelope. Figure 10 shows the results based on the application of this regulation to maneuvering envelopes without flaps, and gust envelopes. These two graphs indicate boundaries the aircraft should not cross during flight, and the structure must bear all the loads transmitted to the aircraft at whichever point in the diagrams, with the contours being the operational structural limits of the aircraft.

It should be clarified that the gust envelope was obtained by maintaining the load factor derived from applying the regulations for the maneuver limit positive load factor—but, in this case, for a combination of wing load and gust intensity that causes the aircraft to enter a stall condition.

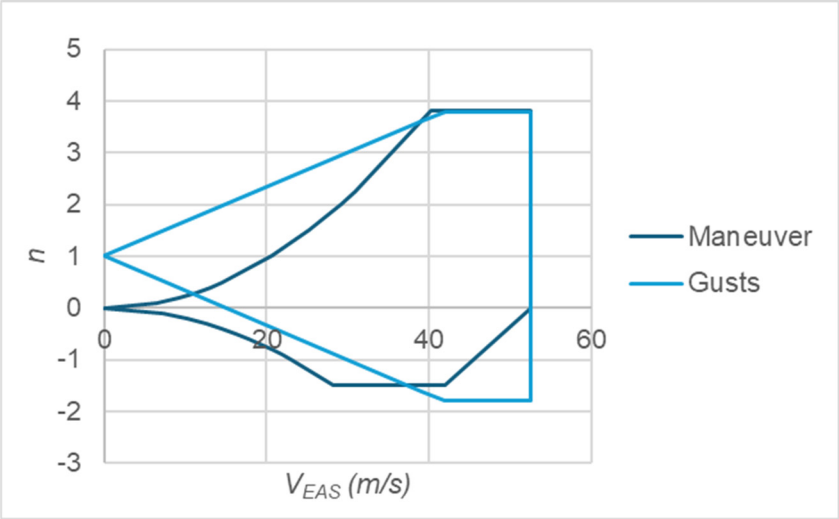

Figure 10. Maneuver envelope and gust envelope.

3.7. Structural Concept

3.7.1. Load Cases

The main structural elements to be sized were the wings. Although the loads supported by each wing are different, in order to simplify the manufacturing process, both wings, front and rear, were designed for the same load cases and, consequently, with the same structure. Another aspect considered at this point was the capacity to operate the UAS as a quadrotor or fixed-wing aircraft. In the case of a quadrotor, the loading state can be reduced to the vertical punctual forces at the tips of the wings. These punctual forces are the resulting force between vertical thrust and motor weight. However, in the case of fixed-wing flights, the load cases are more complicated. Taking the maneuver envelope determined previously into account, the following set of load cases was considered to size the structure:

1. A symmetric maneuver with the limit positive load factor at cruising speed;
2. A symmetric maneuver with the limit negative load factor at cruising speed;
3. Vertical gust with a positive load factor at design speed;
4. Vertical gust with a negative load factor at design speed;
5. An asymmetric maneuver with 2/3 of the limit positive load factor at maneuver design speed, with a steady turn with maximum deflection of the ailerons;
6. An Asymmetric maneuver with 2/3 of the limit negative load factor at maneuver design speed, with a steady turn with maximum deflection of the ailerons;
7. Axial flight as a quadrotor with a load factor equal to 1.2.

All these load cases were simulated with the aid of Tornado software, version 135 [44], excluding the seventh case, which can be calculated analytically. In both flight modes, the structural weight of the wing itself alleviates the loads to be borne because its contribution opposes the aerodynamic and thrust contributions. The drawback is that the structure has not been designed yet, so some hypotheses must be made in order to account for this contribution. As a first approximation, by means of a second-class method, the wing weight was predicted [30], with the result being approximately 900 g. Thus, it was supposed that this weight is distributed along the wingspan as a function of the chord to the power of 1.2. This hypothesis should be evaluated once the structure has been manufactured. Figures 11–13 illustrate the bending moment, shear force, and torsion moment, respectively, for all the load cases considered.

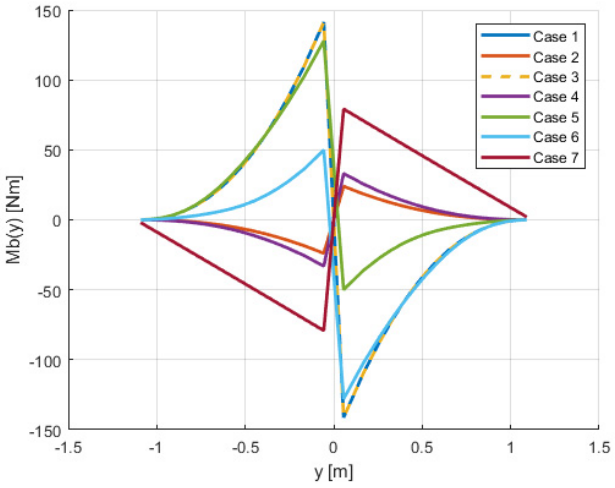

Figure 11. Bending moment introduced for the front wing for the seven load cases considered.

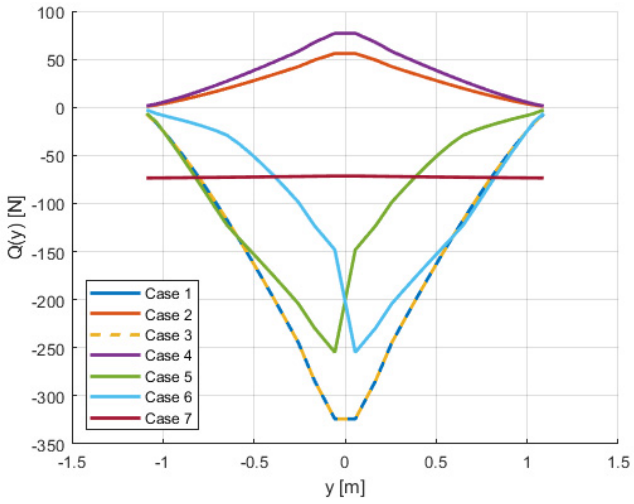

Figure 12. Shear force introduced for the front wing for the seven load cases considered.

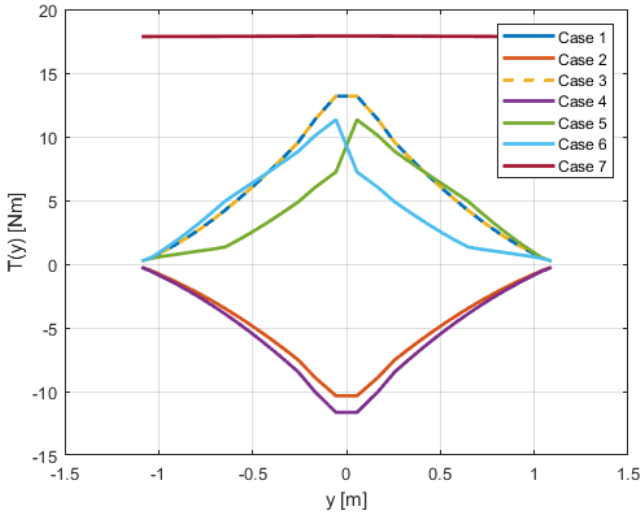

Figure 13. Torsion moment introduced for the front wing for the seven load cases considered.

First, it is necessary to clarify that cases 1 and 3 are overlapping because of the way the gust envelope was developed, i.e., by imposing the positive limit maneuvering load factor. Based on the results of the simulations, the critical load cases are 1, 5, and 7. Case 5 corresponds to a steady turn with a bank angle of approximately 66°, with maximum

aileron deflection. It is important to highlight that in some situations, case 6 is critical, but it is precisely the symmetric counterpart of case 5. Therefore, these cases are essentially equivalent. Case 1 corresponds to a symmetric maneuver at the positive limit load factor. The figures show that these two critical cases, 1 and 5, arising from the operation of the UAS as a fixed-wing aircraft, nearly overlap, while in quadcopter mode, the loads are particularly critical in terms of torsion and in the area near the leading edge.

Bearing all this in mind, in the next section, we will explain how the structure is dimensioned based on the manufacturing method to support these loads.

3.7.2. Sizing and Manufacturing

The internal structure of the four half-wings is based on the semi-monocoque structural concept, including skin, spars, ribs, and stringers, each playing a distinct structural role. Stringers are co-cured on the skin (manufactured in a single curing process), and the spar and ribs are assembled through a secondary bonding process pertaining to the components previously manufactured. The skin defines the aerodynamic contours of the wing, while the spars primarily bear bending loads. The ribs serve to transfer torsional loads to the spars, and the stringers reinforce the skin to prevent buckling. To determine the optimal number and distribution of these elements, a finite element structural analysis is required. Given that the half-wing structure is entirely composed of composite materials, this analysis will focus on defining the stacking sequences for each structural component.

To ensure the structural analysis is accurate, appropriate boundary conditions and representative load cases must be defined. The half-wing is typically modeled with a clamped boundary condition at the wing root. In this case, the half-wings are connected to the fuselage by means of a detachable joint through holes at the ends of the spars. Therefore, the clamped condition will be imposed at the nodes of these holes, restricting all the degrees of freedom. This approach increases the stresses in the joint zone, yielding conservative results regarding material failure indices.

The structural sizing load case is determined as a combination of the critical cases identified in Section 3.6.1, with cases 1 and 5 being the most restrictive for bending and vertical loads, while case 7 imposes the most significant torsional constraints. Distributed aerodynamic loads were replaced with an equivalent point load that produces the same bending and torsional effects in order to allow validation using a structural test bench later.

For the equivalent bending and vertical load calculations, the wing was approximated as a cantilever beam with an embedded root and a concentrated vertical load at the tip, equivalent to the maximum vertical load of 225 N. This load generates a bending moment of 247.5 Nm at the root, exceeding all values obtained in the bending moment distribution curves. This simplification leads to a conservative structural design, ensuring a safety margin relative to the maximum limit loads. To incorporate the bending moment, the application point of the load is displaced by 78 mm from the quarter–chord axis, introducing a torque of 17.5 Nm. The resulting load is applied at the holes interfacing with the motor and the longitudinal members at the wingtip.

Upon completing the finite element analysis using MSC Apex, version 2024.1, for meshing and Nastran, version 2024.1, as a solver, we obtained the structural configuration shown in Figures 14 and 15. Figure 14 illustrates the front (brown) and rear (cyan) spars enclosing the ribs (gray), with all the components incorporating fins to ensure proper stress continuity. Additionally, the lower surface (green) and upper surface (salmon) stringers are depicted, contributing to the structural reinforcement of the wing.

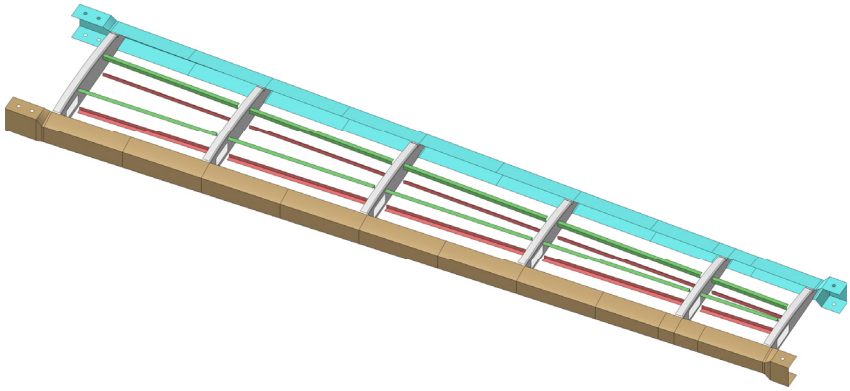

Figure 14. Internal wing structure.

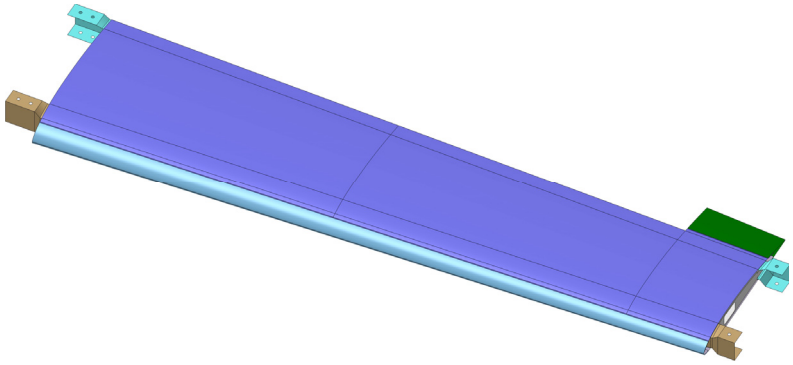

Figure 15. External wing elements.

Figure 15 presents the various components that constitute the wing skin, including the leading edge (blue), outer skin (violet), and trailing edge (forest green). These elements are designed to ensure aerodynamic efficiency and structural integrity while distributing loads effectively across the half-wing.

The rear spar maintains a constant thickness of nine plies ([45, −45, 0, 90]s, odd symmetry), providing structural stability. Additionally, the number and placement of ribs and stringers were determined to prevent skin buckling, resulting in a total of five ribs and two stringers per bay. The skin, stringers, and ribs were constructed with a balanced symmetrical laminate of [45, −45]s to ensure structural consistency and good resistance to impacts.

The results of the structural analysis are presented in Figures 16–18. Figure 16 illustrates the displacement of the structure under the applied load, providing insight into its overall deformation behavior. Figure 17 depicts the failure index distribution based on the Hill criterion, specifically in the root joint region, where the highest stress concentrations occur. However, stress concentration has a failure index (i.e., the value at which a composite material fails) smaller than 1.0 in all the layers, so loads are far from being critical. Lastly, Figure 18 presents the first buckling mode of the structure, revealing that the skin experiences buckling in the unsupported region between the stringers in the section closest to the embedment. The final weight of the half-wing is 877 g, which is lower than that supposed for load estimation.

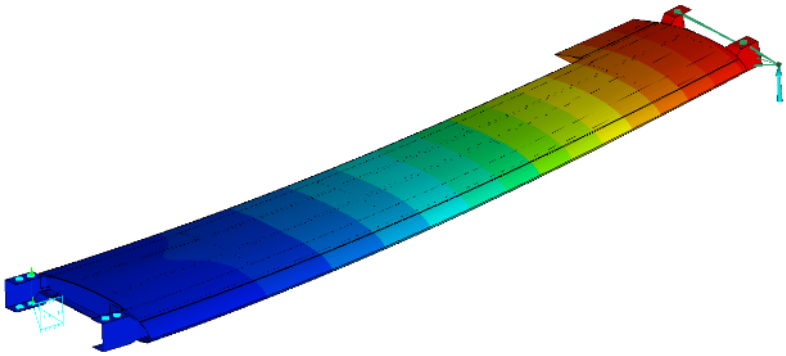

Figure 16. Displacement field of the structure in the analyzed load case. Maximum (red) = 27 mm; minimum (blue) = 0 mm.

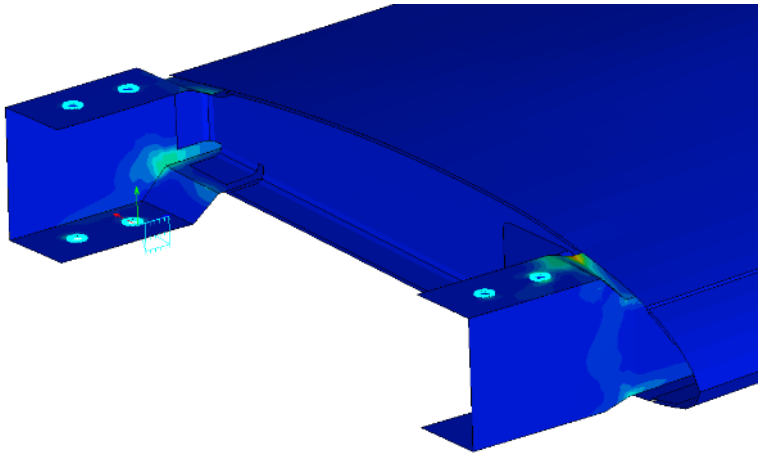

Figure 17. Details of the failure index of the material in the area of the root joint bolts (higher values). Maximum (red) = 0.273; minimum (blue) = 4×10^{-4}.

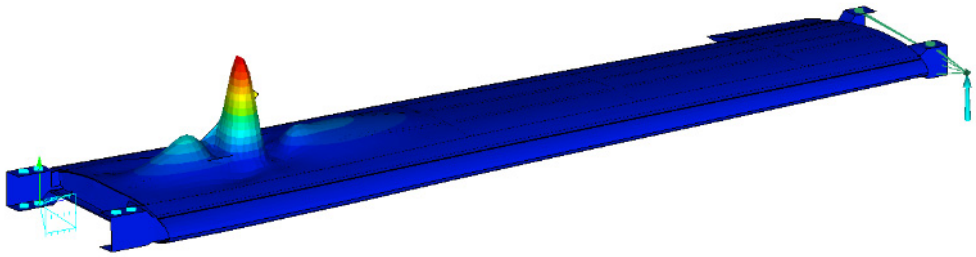

Figure 18. The first buckling mode in the loading direction with a buckling factor of 1.4.

The use of molds is essential in the manufacture of composite components in order to ensure precise geometry, structural integrity, and surface quality. Molds provide a controlled framework that maintains the desired shape of a composite material during the curing process, preventing deformations and inconsistencies. Additionally, they facilitate the proper layering and compaction of fiber-reinforced laminates, ensuring they have optimal mechanical properties. Given the complexity of composite manufacturing, molds also help achieve repeatability and accuracy in production, crucial for aerospace applications where stringent dimensional and performance requirements must be met.

During the development of this process, it was necessary to manufacture molds for the subsequent fabrication of the composite components. A 3D-printing-based technique was employed for mold fabrication, utilizing a large-format printer ($1000 \times 500 \times 400$ mm^3 printable volume) that enabled the production of the largest component models as single pieces (Figure 19). The process began with the printing of a pattern replicating the final part's geometry. To enhance surface quality, the pattern underwent a finishing treatment

that included sanding (Figure 20) and the application of XCR epoxy resin [45] (Figure 21), ensuring that any imperfections were not transferred to the mold. A release agent was then applied to facilitate the separation of the mold from the pattern.

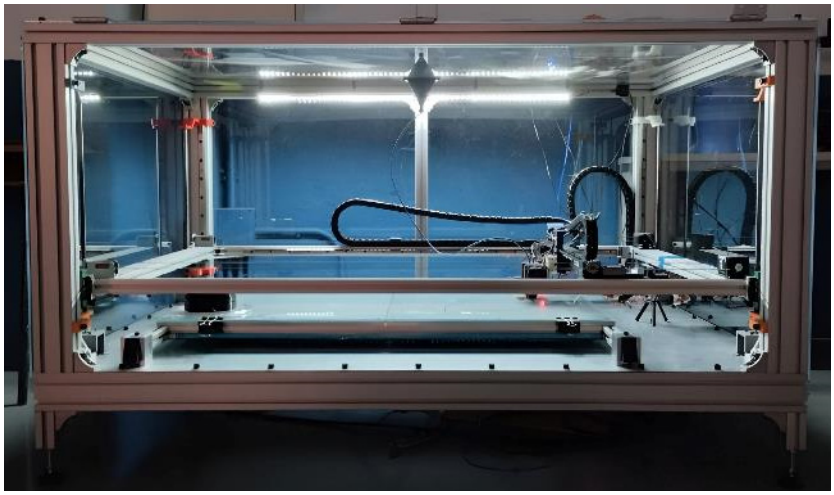

Figure 19. Large-format 3D printer used in mold manufacturing.

Figure 20. Sanding of the outer skin pattern surface.

Figure 21. Application of XCR resin on the outer skin pattern surface.

The next step of the mold manufacturing process was the application of an EG160 gel coat [46] on the pattern's surface (Figure 22), followed by the reinforcement of the structure using short-glass fiber-reinforced EMP160 resin [47] (Figure 23). This combination provides the mold with the mechanical strength it requires. A key advantage of using EG160 and EMP160 is their two-stage curing process: an initial curing phase at room temperature, followed by a post-curing phase after demolding, reaching the operational temperature

limit of 160 °C (Figure 24). This approach allows for the use of low-performance printing materials, such as PLA, while still achieving high-temperature-resistant molds.

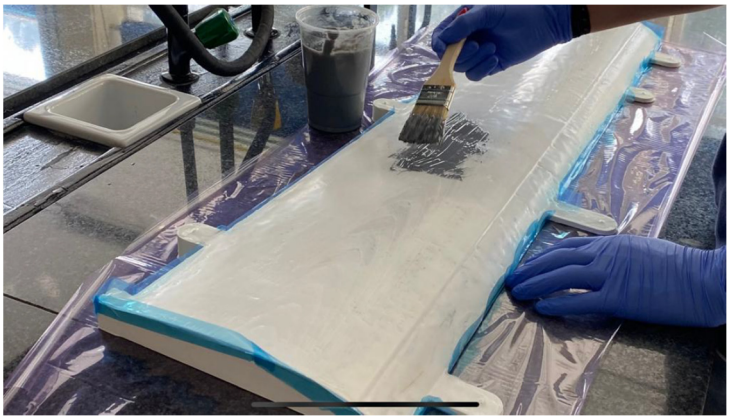

Figure 22. Application of EG160 resin on the outer skin pattern surface.

Figure 23. Application of EMP160 resin on the outer skin pattern surface.

Figure 24. Final outer skin mold.

After the molds were fabricated, all the wing components were laminated according to the ply sequences derived from the structural analysis and subsequently cured. As EMP160 resin has a maximum service temperature of 160 °C, the initial curing was performed under a vacuum at 155 °C for three hours in order to ensure the transfer of the geometry between the tool and the composite. Following demolding, a post-curing process was conducted at 180 °C for two hours to achieve full curing, enhancing the mechanical properties and thermal stability of the components.

Finally, the laminated components were assembled using Araldite AW 113 adhesive, ensuring structural integrity and load transfer between elements. This assembly process resulted in the final structure shown in Figure 25.

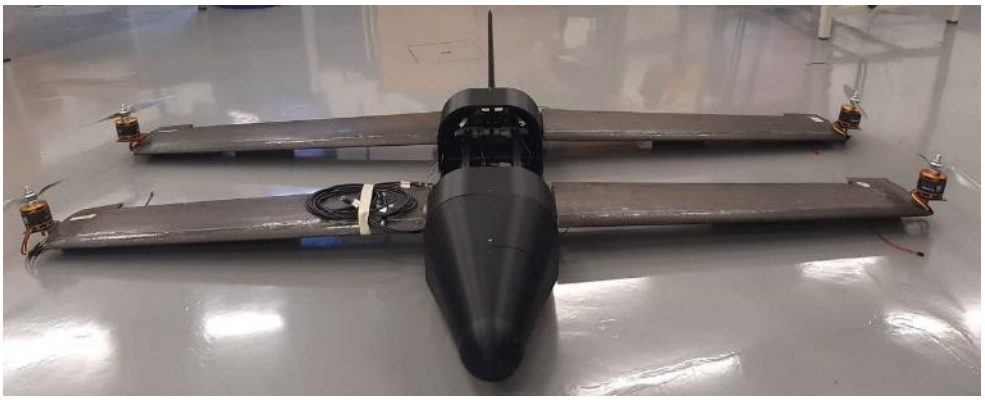

Figure 25. Final integration of the wings with the fuselage.

4. Discussion

We have presented a conceptual design methodology for a small UAS based on the classic aircraft design models used for manned aircraft. This approach allows for more critical decision making in the design process, as opposed to the typical approach for this type of aircraft, which relies on previous experience in the world of model aircraft.

However, the extrapolation of these methods must be validated in greater depth to ensure their complete validity within the precision margins sought in the conceptual design process. Therefore, we sought to manufacture an aircraft in order to subsequently validate the propulsion models, aerodynamic models, and weight estimations used through testing.

The results obtained from the first manufacturing trials suggest that the weight estimation models, at least in this case, were suitably adapted, as the results were conservative. It is true that the materials used are typical of the aerospace industry, and there are existing recommendations on how to adapt these weight estimation models [32], but they have not been applied to such small aircraft before this study. The structural weight estimation of the wing was 907 g, and the weight obtained after the structural design was 877 g, which corresponds to a deviation of 3.4%.

A major difficulty we encountered was the application of the gust model. These aircraft, which fly at low wing loads and moderate speeds, are not capable of withstanding the gust intensities specified in the military standards for unmanned aircraft certification without stalling. This issue is not explicitly addressed in the standards, and the solution employed to adapt the model is merely a proposal. Further reflection on the advantages and disadvantages would be necessary to ensure that the approach adopted is optimal. The key is to find a balance between the structural requirements and the wing load demands. Again, based on the initial manufacturing tests, the structural solution seems to handle the loading conditions quite well, which would allow it to withstand gust-induced loads, even though it was not explicitly designed for this purpose. Nevertheless, a sensitivity study could be carried out to assess how the modification of the vertical gust limit affects the wing loading in case it is possible to lower the load factor for which the structure is to be designed, especially if the manufacturing method and materials used are not based on high-performance composite materials like those employed in this project.

Another important issue is that the use of the equipment list provided by the Cargo Drone Challenge competition, held in 2016, may mean that the weights and fuselage size were overestimated. Technology advances at a rapid pace, and, currently, equipment that performs the same functions and yet is smaller, lighter, and consumes less energy can be

found. However, this does not diminish the viability of the solution found; rather, it raises the question of whether a more optimized solution, better suited to the current equipment market, could have been found.

5. Conclusions

This work presents a case study of applying classical conceptual and preliminary design models of aircraft to the sizing of a lightweight drone weighing less than 25 kg at maximum takeoff weight with an electric motor. The challenges of adapting these methodologies to the small scale of such aircraft are highlighted. This is evident in the significant variability of the results obtained when applying different aerodynamic models, for example. To assess the reliability of these results, it will be necessary to conduct experimental verifications through wind tunnel tests as a first step. However, given the lack of existing conceptual design models developed specifically for this type of aircraft, a successful adaptation of classic methodologies has been achieved, allowing for the development of a prototype whose performance promises to meet the initial requirements. This represents a very important step forward in establishing reliable models for the conceptual design of UASs in the mini category.

Despite these challenges, progress has been made in the structural sizing of the wing, to the point of fabricating a preliminary prototype of the aircraft, which is yet to be equipped with the avionics needed for autonomous flight. We confirmed that the proposed structural design can withstand the considered loads and that the weight estimation obtained using class 2 models adapted quite accurately to the final weight of the wing structure. In relation to the structural design, it is worth highlighting the innovative critical load estimation procedure for structural sizing based on the detailed airworthiness requirements of NATO certification requirements. This ensures that the structure is prepared to withstand maneuvering and gust loading conditions.

Finally, the novel manufacturing process developed in this study allowed us to achieve all the advantages of using high-performance composite materials, typical of manned aircraft, but with the ease of generating molds through additive printing in an agile process and maintaining the required tolerances and structural properties.

As future work, progress should be made on integrating the onboard systems and equipment to enable flight and, as mentioned, conducting tests both in wind tunnels and in flight to verify the validity of adapting classical conceptual design models. Additionally, these tests could lead to the development of new conceptual design methodologies adapted to smaller aircraft of this type.

Author Contributions: Conceptualization, A.S.-C., A.F.L. and C.C.-R.; data curation, A.S.-C. and D.d.R.V.; formal analysis, A.S.-C., D.d.R.V., A.F.L. and C.C.-R.; funding acquisition, A.F.L.; investigation, A.S.-C., D.d.R.V., A.F.L. and C.C.-R.; methodology, A.S.-C., D.d.R.V., A.F.L. and C.C.-R.; project administration, A.F.L.; resources, A.S.-C. and C.C.-R.; software, A.S.-C. and D.d.R.V.; supervision, A.F.L. and C.C.-R.; validation, A.F.L. and C.C.-R.; visualization, A.S.-C., D.d.R.V., A.F.L. and C.C.-R.; writing—original draft, A.S.-C., D.d.R.V. and C.C.-R.; writing—review and editing, A.S.-C., D.d.R.V. and C.C.-R. All authors have read and agreed to the published version of the manuscript.

Funding: This project received funding from the National Research Program Retos de la Sociedad under the Project STARGATE: Desarrollo de un sistema de monitorización estructural basado en un microinterrogador y redes neuronales (reference PID2019-105293RB-C21).

Data Availability Statement: The original contributions presented in this study are included in the article. Further inquiries can be directed to the corresponding author.

Acknowledgments: The authors would like to thank the team members who participated in the Airbus Cargo Drone Challenge for their contributions.

Conflicts of Interest: The authors declare no conflict of interest.

References

1. Gundlach, J. *Civil and Commercial Unmanned Aircraft Systems*; AIAA Education Series: Reston, VA, USA, 2016.
2. Gundlach, J. *Designing Unmanned Aircraft Systems: A Comprehensive Approach*, 1st ed.; AIAA Educational Series: Reston, VA, USA, 2014.
3. Austin, R. *Unmanned Aircraft Systems*; Willey: Hoboken, NJ, USA, 2010.
4. Gómez-Rodríguez, Á.; Sanchez-Carmona, A.; García-Hernández, L.; Cuerno-Rejado, C. Preliminary Correlations for Remotely Piloted Aircraft Systems Sizing. *Aerospace* **2018**, *5*, 5. [CrossRef]
5. Cuerno-Rejado, C.; García-Hernández, L.; Sánchez-Carmona, A.; Carrio, A.; Sanchez-Lopez, J.L.; Campoy, P. Historical evolution of the unmanned aerial vehicles to the present. *Dyna* **2016**, *91*, 282–288.
6. Elmeseiry, N.; Alshaer, N.; Ismail, T. A Detailed Survey and Future Directions of Unmanned Aerial Vehicles (UAVs) with Potential Applications. *Aerospace* **2021**, *8*, 363. [CrossRef]
7. Goraj, Z. Design challenges associated with development of a new generation UAV. *Aircr. Eng. Aerosp. Technol.* **2005**, *77*, 361–368. [CrossRef]
8. EASA Drones & Air Mobility. Available online: https://www.easa.europa.eu/en/domains/civil-drones (accessed on 27 February 2025).
9. FAA Drones. Available online: https://www.faa.gov/uas (accessed on 27 February 2025).
10. Panagiotou, P.; Kaparos, P.; Salpingidou, C.; Yakinthos, K. Aerodynamic design of a MALE UAV. *Aerosp. Sci. Technol.* **2016**, *50*, 127–138. [CrossRef]
11. Kontogiannis, S.G.; Ekaterinaris, J.A. Design, performance evaluation and optimization of a UAV. *Aerosp. Sci. Technol.* **2013**, *29*, 339–350. [CrossRef]
12. Bravo-Mosquera, P.D.; Botero-Bolivar, L.; Acevedo-Giraldo, D.; Cerón-Muñoz, H.D. Aerodynamic design analysis of a UAV for superficial research of volcanic environments. *Aerosp. Sci. Technol.* **2017**, *70*, 600–614. [CrossRef]
13. Goetzendorf-Grabowski, T.; Rodzewicz, M. Design of UAV for photogrammetric mission in Antarctic area. *Proc. Inst. Mech. Eng. Part G J. Aerosp. Eng.* **2017**, *231*, 1660–1675. [CrossRef]
14. Panagiotou, P.; Fotiadis-Karras, S.; Yakinthos, K. Conceptual design of a Blended Wing Body MALE UAV. *Aerosp. Sci. Technol.* **2018**, *73*, 32–47. [CrossRef]
15. Cipolla, V.; Dine, A.; Viti, A.; Binante, V. MDAO and Aeroelastic Analyses of Small Solar-Powered UAVs with Box-Wing and Tandem-Wing Architectures. *Aerospace* **2023**, *10*, 105. [CrossRef]
16. Zhao, X.; Zhou, Z.; Zhu, X.; Guo, A. Design of a Hand-Launched Solar-Powered Unmanned Aerial Vehicle (UAV) System for Plateau. *Appl. Sci.* **2020**, *10*, 1300. [CrossRef]
17. An, J.H.; Kwon, D.Y.; Jeon, K.S.; Tyan, M.; Lee, J.W. Advanced Sizing Methodology for a Multi-Mode eVTOL UAV Powered by a Hydrogen Fuel Cell and Battery. *Aerospace* **2022**, *9*, 71. [CrossRef]
18. Suewatanakul, S.; Porcarelli, A.; Olsson, A.; Grimler, H.; Chiche, A.; Mariani, R.; Lindbergh, G. Conceptual Design of a Hybrid Hydrogen Fuel Cell/Battery Blended-Wing-Body Unmanned Aerial Vehicle—An Overview. *Aerospace* **2022**, *9*, 275. [CrossRef]
19. Bishay, P.L.; Kok, J.S.; Ferrusquilla, L.J.; Espinoza, B.M.; Heness, A.; Buendia, A.; Zadoorian, S.; Lacson, P.; Ortiz, J.D.; Basilio, R.; et al. Design and Analysis of MataMorph-3: A Fully Morphing UAV with Camber-Morphing Wings and Tail Stabilizers. *Aerospace* **2022**, *9*, 382. [CrossRef]
20. Airbus Cargo Drone Challenge. Available online: https://www.airbus.com/en/newsroom/press-releases/2016-07-airbus-group-and-local-motors-name-winners-of-next-generation (accessed on 11 March 2025).
21. Torenbeek, E. *Synthesis of Subsonic Airplane Design*; Delft University Press: Delft, The Netherlands; Kluwer Academic Publishers: Dordrecht, The Netherlands, 1982.
22. Roskam, J. *Airplane Design, Part I: Preliminary Sizing of Airplanes*; Roskam Aviation and Engineering Corporation: Ottawa, KS, USA, 1985.
23. Roskam, J. *Airplane Design, Part II: Preliminary Configuration Design and Integration of the Propulsion System*, 1st ed.; Roskam Aviation and Engineering Corporation: Ottawa, KS, USA, 1989.
24. Roskam, J. *Airplane Design, Part III: Layout Design of Cockpit, Fuselage, Wing and Empennage: Cutaways and Inboard Profiles*; Roskam Aviation and Engineering Corporation: Ottawa, KS, USA, 1986.
25. Roskam, J. *Airplane Design, Part IV: Layout Design of Landing Gear and Systems*; Roskam Aviation and Engineering Corporation: Ottawa, KS, USA, 1986.
26. Roskam, J. *Airplane Deisgn. Part V: Component Weight Estimation*; DAR Corporation: Ottawa, KS, USA, 1999; ISBN 1884885500.
27. Roskam, J. *Airplane Design, Part VI: Preliminary Calculation of Aerodynamic, Thrust and Power Characteristics*; Roskam Aviation and Engineering Corporation: Ottawa, KS, USA, 1987.

28. Roskam, J. *Airplane Design, Part VII: Determination of Stability, Control and Performance Characteristics: FAR and Military Requirements*; Roskam Aviation and Engineering Corporation: Ottawa, KS, USA, 1988.
29. Roskam, J. *Airplane Deisgn, Part VIII: Airplane Cost Estimation: Design, Development, Manufacturing And operating*; Roskam Aviation and Engineering Corporation: Ottawa, KS, USA, 1985.
30. Raymer, D.P. *Aircraft design: A Conceptual Approach*, 4th ed.; AIAA: Reston, VA, USA, 2006.
31. NATO. *STANAG 4703/AEP-83 Light Unmanned Aircraft*; Edition B Version 1; Nato Standardization Agency: Brussels, Belgium, 2016.
32. Torenbeek, E. *Advanced Aircraft Design*; John Wiley & Sons, Ltd.: Chichester, UK, 2013.
33. Cuerno-Rejado, C.; García-Hernández, L.; Sanchez-Carmona, A.; Fernández-López, A.; Pintado-Sanjuanbenito, J.M. Diseño Modular de un Rpas de ala Tándem de Despegue Vertical. In Proceedings of the CivilDRON'17, Fundación de la Energía de la Comunidad de Madrid, Madrid, Spain, 25–26 January 2017.
34. Nicolai, L.M.; Carichner, G.E. *Fundamentals of Aircraft and Airship Design*; AIAA Education Series: Reston, VA, USA, 2020; Volume I-Aircraft Design, ISBN 9789896540821.
35. Pratt, K.G. *A Revised Formula for Calculation of Gust Loads*; NACA-TN-2964; NACA: Boston, MA, USA, 1953.
36. Roskam, J. *Airplane Flight Dynamics and Automatic Flight Controls. Part I and II*; Roskam Aviation and Engineering Corporation, USA: Ottawa, KS, USA, 1982.
37. Finck, R.D. USAF Stability and Control DATCOM. *Flight Dyn. Labaratory* **1978**, *18*, 3200.
38. Kheit, E. Software Development and Validation for Subsonic and Transonic Aircraft Class 2 Drag Polar Determination. In Proceedings of the 18th International Congress of Mechanical Engineering, Ouro Preto, MG, Brazil, 6–11 November 2005.
39. Roskam, J. *Methods for Estimating Stability and Control Derivatives of Conventional Subsonic Airplanes*, 4th ed.; Roskam Aviation and Engineering Corporation: Ottawa, KS, USA, 1983.
40. Drela, M. AVL (Athena Vortex Lattice). Available online: https://web.mit.edu/drela/Public/web/avl/ (accessed on 6 April 2025).
41. APC. Propeller Performance Data. Available online: https://www.apcprop.com/technical-information/performance-data/ (accessed on 4 March 2025).
42. AXi Model Motors. Available online: https://www.modelmotors.cz/product/motors/ (accessed on 4 March 2025).
43. e-calc. Available online: https://www.ecalc.ch/ (accessed on 4 March 2025).
44. Melin, T. A Vortex Lattice MATLAB Implementation for Linear Aerodynamic Wing Applications. Master's Thesis, Royal Institute of Technology (KTH), Stockholm, Sweden, 2000.
45. Easycomposites. XCRTM Epoxy Coating Resin—Technical Datasheet 2024. Available online: https://media.easycomposites.co.uk/datasheets/EC-TDS-XCR-Epoxy-Coating-Resin.pdf (accessed on 13 April 2025).
46. Easycomposites. EG160 High Temp Epoxy Tooling Gelcoat—Technical Datasheet 2023. Available online: https://media.easycomposites.co.uk/datasheets/EG160-High-Temp-Epoxy-Tooling-Gelcoat-v2.pdf (accessed on 13 April 2025).
47. Esaycomposites. EMP160 High Temperature Moulding Paste—Technical Datasheet 2024. Available online: https://media.easycomposites.eu/datasheets/EC-TDS-EMP160-High-Temp-Moulding-Paste.pdf (accessed on 13 April 2025).